Separation and Purification Technology 371 (2025) 133312

Contents lists available at ScienceDirect

Separation and Purification Technology

journal homepage: www.elsevier.com/locate/seppur

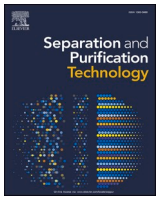

Ultra-fast Joule heating synthesis of homogeneous copper-based bimetallic catalysts for electrochemical nitrate-to-ammonium reduction in wastewater treatment☆

Jenn Fang Su [a,b,c,*], Minh-Son Hoang [a,d], Herma Dina Setiabudi [e,f]

[a] Department of Chemical and Materials Engineering, Chang Gung University, Taoyuan 33302, Taiwan
[b] Center for Sustainability and Energy Technologies, Chang Gung University, Taoyuan 33302, Taiwan
[c] Division of Hematology and Oncology, Department of Internal Medicine, Chang Gung Memorial Hospital at Linkou, Taoyuan 333, Taiwan
[d] Faculty of Chemical Engineering, Industrial University of Ho Chi Minh City, Ho Chi Minh City 700000, Viet Nam
[e] Faculty of Chemical & Process Engineering Technology, Universiti Malaysia Pahang Al-Sultan Abdullah, Lebuh Persiaran Tun Khalil Yaakob, 26300 Gambang, Pahang, Malaysia
[f] Centre for Research in Advanced Fluid & Processes, Universiti Malaysia Pahang Al-Sultan Abdullah, Lebuh Persiaran Tun Khalil Yaakob, 26300 Gambang, Pahang, Malaysia

ARTICLE INFO

Editor: B. Van der Bruggen

Keywords:
Joule heating
Homogeneous bimetal
Metal catalyst
Nitrate reduction
Ammonia
Water treatment

ABSTRACT

The conversion of nitrate to ammonia presents a promising solution to reduce the energy consumption and carbon footprint associated with the traditional Haber-Bosch process, while also addressing the environmental impacts of nitrate-containing wastewater. To tackle the challenges in catalyst preparation for efficient electrochemical nitrate reduction toward ammonium, this study reports an extremely rapid Joule-heating synthetic method to fabricate a series of copper (Cu)-based bimetallic catalysts. The results demonstrate that the Joule-heating process leads to the formation of well-dispersed and homogeneous bimetallic particles as evidenced by the scanning electron microscope (SEM) and corresponding energy dispersive spectroscopy (EDS), exhibiting an enhanced catalytic activity. Among various samples, the homogeneous copper-nickel (CuNi) catalyst presents an exceptional ammonium selectivity of 98 %, an ammonium yield of 49 %, and an ammonium formation rate of 764 μg h^{-1} cm^{-2}, which are approximately 2 times higher than Cu monometallic catalyst. This superior activity is attributed to the increased electrochemical active surface area (ECSA) in CuNi materials. Additionally, X-ray photoelectron spectroscopy (XPS) characterization confirms the electronic redistribution within the CuNi structure, revealing a lower oxidation state of Cu, which further contributes to the improved efficiency in the nitrate reduction reaction. Overall, this study enables a new route for the rational design of homogenous bimetallic catalysts in nitrate reduction for wastewater treatment and environmental protection.

1. Introduction

Ammonia (NH_3) is recognized as a crucial material for the development of modern society [1]. It is currently the second most produced compound globally and is extensively utilized across various industries, including textiles, agriculture, food and beverages, pharmaceuticals, water treatment, rubber, papermaking, and chemical industry [2]. Additionally, NH_3 holds significant promise as a potential carbon-free energy source, primarily due to its ability to serve as an efficient hydrogen (H_2) carrier. It can be readily decomposed into H_2 through thermolytic processes or catalytic reactions, making it a practical medium for H_2 delivery [3]. In addition to its high energy density, NH_3 offers considerable advantages in terms of storage and transportation. Unlike liquid H_2, which requires extremely low temperatures or high-pressure containment, NH_3 can be stored and transported under normal conditions. These characteristics position NH_3 as a compelling candidate for sustainable, low-cost, and carbon-free energy applications [4,5]. Currently, the manufacture of NH_3 predominantly relies on the Haber-Bosch process, which is heavily dependent on fossil filed (used for generating H_2 from CH_4) and requires high temperature and pressure,

☆ This article is part of a special issue entitled: 'CESE2024-ICARE' published in Separation and Purification Technology.

* Corresponding author at: No. 259 Wenhua 1st Road, Guishan District, Taoyuan 33302, Taiwan.
E-mail address: jennfangsu@mail.cgu.edu.tw (J.F. Su).

https://doi.org/10.1016/j.seppur.2025.133312
Received 20 March 2025; Received in revised form 21 April 2025; Accepted 29 April 2025
Available online 29 April 2025

thereby contributing to significant environmental pollution [6]. Therefore, there is a strong need for the development of a more environmentally friendly and efficient method for NH_3 production.

In recent years, the electrochemical synthesis of ammonia (NH_3) from nitrogen gas (N_2) under ambient conditions has received much attention [7–9]. However, the strong triple bond (N≡N) and non-polar nature of N_2 pose substantial challenges, resulting in low conversion efficiency for its electrochemical reduction to NH_3 [10,11]. Conversely, nitrate ion (NO_3^-), which is among the most prevalent water pollutants, becomes an attractive alternative nitrogen source for the electrochemical synthesis of NH_3 [12–15]. However, the extreme complexity of the electrochemical reduction of nitrate (NO_3RR) and nitrite (NO_2RR), involving multiple proton/electron-transfer steps and intermediates, requires an effective catalyst to control selectivity toward the desired product and to drive efficient NH_3 production for industrial purposes. Palladium (Pd), ruthenium (Ru), copper (Cu), and other precious metal-based materials have demonstrated catalytic activity for NO_3RR [16–19]. Among them, Cu-based materials are currently regarded as the most promising catalyst for nitrate conversion, due to their relatively low cost, natural abundance, strong adsorption for nitrogen species, and rapid reduction kinetics [20–23]. Despite their potential for NO_3^- electroreduction, Cu-based materials still face some notable challenges: (i) the deactivation of catalysts due to accumulation of the toxic product, NO_2^-, and oxidation of Cu during the nitrate reduction process [24]; (ii) requirement of high overpotential for NH_3 production from NO_3^- and intense competition from the hydrogen evolution reaction (HER) [25]; (iii) poor adsorption capacity for hydrogen on Cu catalysts, limiting the hydrogenation reaction toward the final NH_3 product [20].

Several reports suggest that introducing a second metal, such as iron (Fe), cobalt (Co), ruthenium (Ru), nickel (Ni), zinc (Zn), and titanium (Ti), can effectively overcome the above-mentioned problems [26–32]. For instance, combining Cu with Fe [33] or Ni [25] can modify the d-band center of the alloy, thus enhancing the adsorption energy of reaction intermediates during NO_3RR. The intrinsic properties of added metals can also enhance the NO_3RR through a synergistic effect, where Cu demonstrates efficient activity in reducing NO_3^- to NO_2^-, while the second metal excels in converting NO_2^- to NH_3 [30,34]. To further enhance the performance of bimetallic catalysts, dispersing the metal atoms into isolated sites offers significant advantages compared to the bulk materials. Key benefits include a high exposure of active sites for the adsorption and conversion of reactants, as well as homogeneous active sites and structures that enable uniform interaction and lead to improved selectivity.

However, achieving a well-dispersed and homogeneous bimetallic catalyst is difficult due to the substantial miscibility gap in the phase diagram [35]. For instance, Cu is thermodynamically miscibility with Pd and Zn, but it remains immiscible with silver (Ag), Ni, and Fe [36]. Traditional methods such as co-reduction, concurrent thermal decomposition, seed-mediated growth, and galvanic replacement only partially generate the bimetallic structure in the form of core–shell or heterostructure [35,37]. These conventional approaches also involve high energy consumption, long reaction times and low production efficiency. Conversely, less common techniques such as spark discharge and pulse laser ablation can mix immiscible elements, but achieving well-dispersed nanoparticles with these techniques requires highly specific and tightly controlled conditions, such as precise operating pressure and carefully chosen media [38,39]. The ultrafast Joule-heating technique presents a promising alternative for synthesizing homogeneous bimetallic catalyst, especially for systems like Cu-Fe or Cu-Ni, which are typically limited by significant miscibility gaps. By delivering a rapid, localized high-temperature environment through a current pulse followed by instant quenching, Joule heating approach is expected to enable efficient decomposition of metal precursors, promote the mixing of otherwise immiscible elements, and stabilizes the resulting bimetallic nanoparticles during the quenching process [40–43]. Despite its potential, the use of Joule heating synthesis in bimetallic catalysts for NO_3RR has not been extensively explored in the literature.

In this study, the Joule heating method was employed to prepare three different homogeneous Cu-based bimetallic catalysts, i.e. CuFe, CuNi, CuPd, as well as the control sample of Cu monometallic catalyst for NO_3RR. The materials characterization through X-ray diffraction (XRD), scanning electron microscopy (SEM), energy dispersive spectroscopy (EDS), and X-ray photoelectron spectroscopy (XPS) was conducted to confirm the homogeneity and formation of bimetallic alloys. The subsequent electrochemical evaluation of Cu-based monometallic and bimetallic catalysts via cyclic voltammetry (CV) and a series of constant-potential reactions revealed that all catalysts can generate N_2 and NH_4^+ with limited formation of NO_2^- during the NO_3RR. Among various catalysts, the homogeneous CuNi catalyst exhibit superior reduction performance, which can be attributed to the increased electrochemical surface area (ECSA), improved NO_3^- to NO_2^- conversion, and favored hydrogenation pathway toward NH_4^+ production. To the best of our knowledge, this work represents the first report to employ the Joule-heating method for the synthesis of a range of Cu-based catalysts and to evaluate their performance in NO_3RR, offering a scalable strategy and rational design of catalysts for environmental applications.

2. Materials and methods

2.1. Materials

Anhydrous $CuCl_2$ (98 %) was obtained from Thermo Scientific (USA). $PdCl_2$ (99 %) and $NaNO_3$ were purchased from Sigma-Aldrich (USA). $NiCl_2{\cdot}6H_2O$ (98 %) was provided by Alfa Aesar (USA), while $FeCl_3{\cdot}6H_2O$ (98 %) was sourced from Acros Organic (Belgium). Isopropyl alcohol (IPA), $HClO_4$, and Nafion (perfluorinated resin solution) (10 % in H_2O) were also obtained from Sigma-Aldrich (USA). All reagents were used without further purification.

2.2. Metallic catalyst preparation

The Cu, CuFe, CuNi, and CuPd catalysts were prepared from different metal salts ($CuCl_2$, $PdCl_2$, $NiCl_2{\cdot}6H_2O$, and $FeCl_3{\cdot}6H_2O$) through the Joule heating method under ambient environment. A programmable power supply (PPM-7503, Twintex Instrument Ltd.) was used to provide the current pulse. The metal salts were first dissolved in IPA to achieve a concentration of 0.05 M. For bimetallic samples, the molar ratio of Cu to other metals was fixed at 9:1. The metal precursor solution was then dropped onto a carbon holder, i.e. gas diffusion layer (GDL, SGL Sigracet 22BB, Fuel Cell Store), for Joule heating process. The setup for Joule heating process is illustrated in **Fig. S1**. The SEM image for the GDL carbon substrate is provided in **Fig. S2**a. The experiment was conducted using a current of 3.2 A for varying durations. In a preliminary test, the results indicate that a 5-second Joule heating duration is insufficient because large microscale metal precursor particles remain clearly visible on the GDL surface as shown in **Fig. S2**b. Accordingly, the Joule heating duration was set to exceed 6 s in this study to ensure complete decomposition of metal precursors. After completing the process, the metal powder was collected and ground further with a mortar.

2.3. Electrode preparation

3 mg of metal powder were mixed with 3 μL of Nafion and 1.14 mL of IPA using ultrasonic for 30 mins to ensure a well-dispersed catalyst slurry. The slurry was then dropped on a conductive substrate (GDL) until the slurry amount reached 1 mg cm^{-2} on the substrate. The coated electrode was then dried in an oven at 60 °C, and stored in a vacuum chamber before use.

2.4. Materials characterization

X-ray diffraction (XRD) (Brucker D2 phaser) (USA) was utilized for

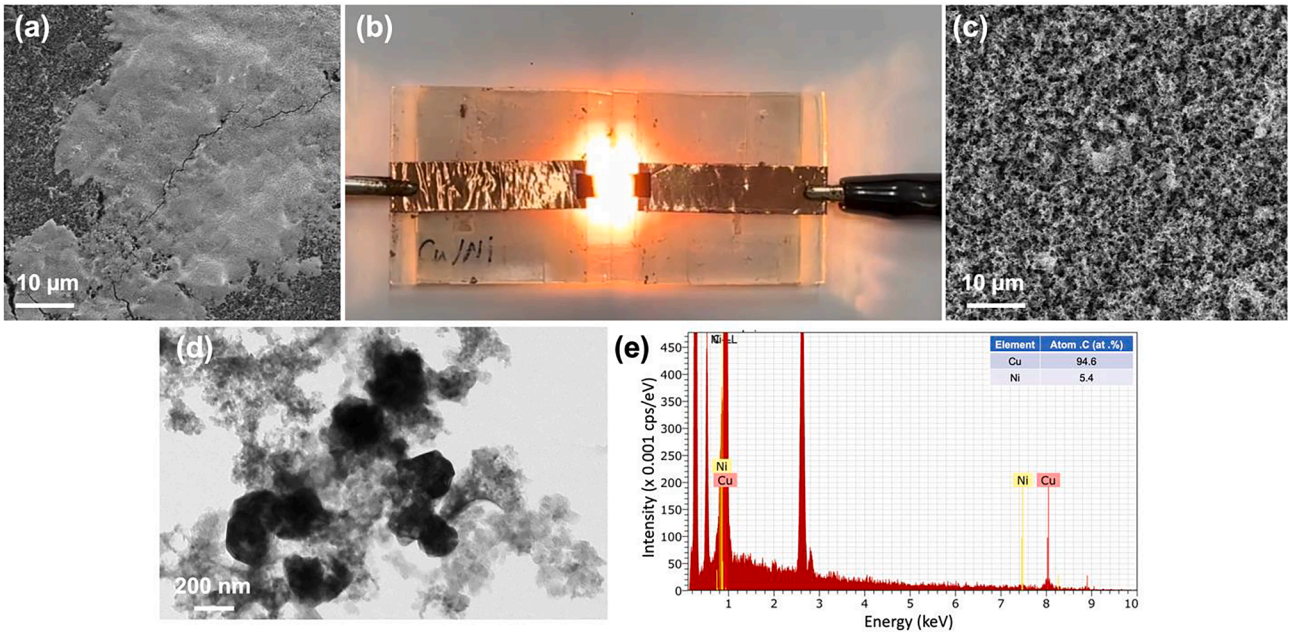

Fig. 1. (a) SEM image of a GDL carbon substrate coated with $CuCl_2$ and $NiCl_2$ salt mixtures. (b) The image of a $CuCl_2$-$NiCl_2$/GDL under joule heating. (c) SEM image of GDL surface with CuNi particles after joule heating. (d) TEM image of collected CuNi particles. (e) Corresponding EDS spectrum of Fig. 1(d) with the element ratio of Cu and Ni provided in the inset.

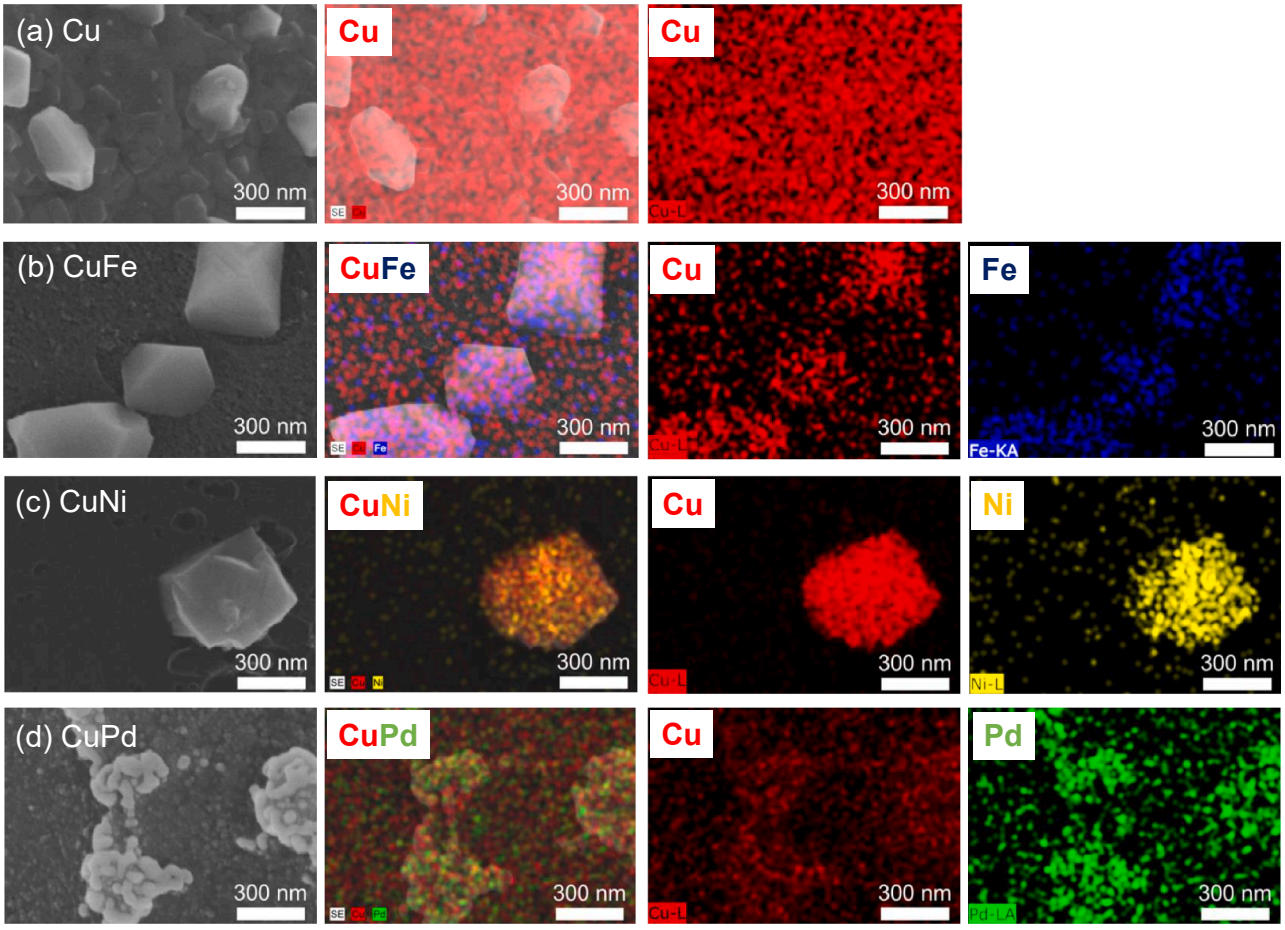

Fig. 2. SEM images and corresponding EDS elements mapping of bimetallic catalysts: (a) CuFe, (b) CuNi, (c) CuPd, and (d) Cu. All bimetallic samples exhibit well distribution of elements.

phase identification. The surface chemical properties of the sample were determined using X-ray photoelectron spectroscopy (XPS) (ULVAC-PHI PHI 5000 Versaprobe II) (Japan). The morphology and size of the sample were sequentially obtained by several instruments such as a scanning electron microscope (SEM) (Hitachi SU800) (Japan) and a high-resolution transmission electron microscope (HR TEM) (JEOL JEM-F200) (Japan). To prepare the TEM samples, the collected metal powder (approximately 0.005 wt%) was dispersed in deionized water (18 mΩ, ELGA PURELAB) and homogenized under 100 W for 1 min. A 5 μL aliquot of the resulting solution was then dropped onto a copper grid (200 mesh), dried in an oven at 80 °C overnight, and stored in a vacuum environment prior to imaging.

2.5. Electrocatalytic nitrate reduction

In this study, an H-type reaction tank was utilized to conduct the electrocatalytic nitrate reduction reaction using a three-electrode system (Fig. S3). The reduction and the oxidation tanks were separated by a Nafion cation exchange membrane (CSE, thickness: 0.16 mm, ASTOM Corporation). A 30 mL solution of 0.1 M $HClO_4$ was prepared for the oxidation tank, containing a platinum rod as the counter electrode. Another 30 mL solution of 0.1 M $HClO_4$ and 0.01 M $NaNO_3$ was prepared for the reduction tank, housing both the working electrode and the reference electrode of the saturated calomel electrode (SCE). The working electrode, prepared as aforementioned, measured 3.0 × 1.0 cm^2, with an effective immersion area of 1.0 × 1.0 cm^2 in the electrolyte. During the 6-hour reaction, different constant voltages (−0.7 V ~ −1.0 V vs SCE) were applied to the working electrode. Magnetic stirrer bars are placed in both tanks to ensure uniform solution concentration throughout the reaction. At each sampling time, a 0.5 mL volume was extracted to measure and record its pH value. To analyze the concentration changes of various substances during the nitrate reduction process under different conditions, ion chromatography and ultraviolet/visible light spectrometry were employed to identify the reactant NO_3^-, intermediate product NO_2^- and the product NH_4^+. The analytical methodology is detailed in **Supporting Information S1**, and the calibration curves for the concentration determination are provided in **Figs. S4 and S5**.

3. Results and discussion

3.1. Catalyst characterization

In this study, various bimetallic particles were prepared as electrocatalysts through a Joule heating process. The schematic for the synthesis of representative bimetallic copper-nickel (CuNi) particles is shown in Fig. 1, while the detailed procedure is described in section 2.2 of Materials and Methods. Typically, the Joule heating process involves the following stages [44]: (1) rapid thermal decomposition of $CuCl_2$ and $NiCl_2$ precursors into Cu and Ni clusters [45], (2) diffusion and mixing of Cu and Ni clusters at elevated temperature, and (3) self-assembly into CuNi particles upon quenching on the surface of the carbon substrate. As shown in Fig. 1a, layers of white deposits, generated from precursor salt particles [36,45], are observed on the surface of GDL carbon substrate after the immersion of metal precursor solution. The precursor-coated GDL is then subjected to the Joule heating process at a current of 3.2 A for a duration of 6 s (Fig. 1b). The intense light emission indicates the high temperature generated during Joule heating. Following the process, the white deposits nearly disappear, revealing a newly formed porous layer on the carbon substrate (Fig. 1c). The TEM image of collected metal powders is provided in Fig. 1d with the particle sizes ranging from 100 to 300 nm. The corresponding energy dispersive spectroscopy (EDS) spectrum (Fig. 1e) confirms that Cu and Ni are the primary components.

It is worth noting that the decomposition temperatures (T_d) of $CuCl_2$ and $NiCl_2$ precursors are about 730 K [46] and 1200 K [47],

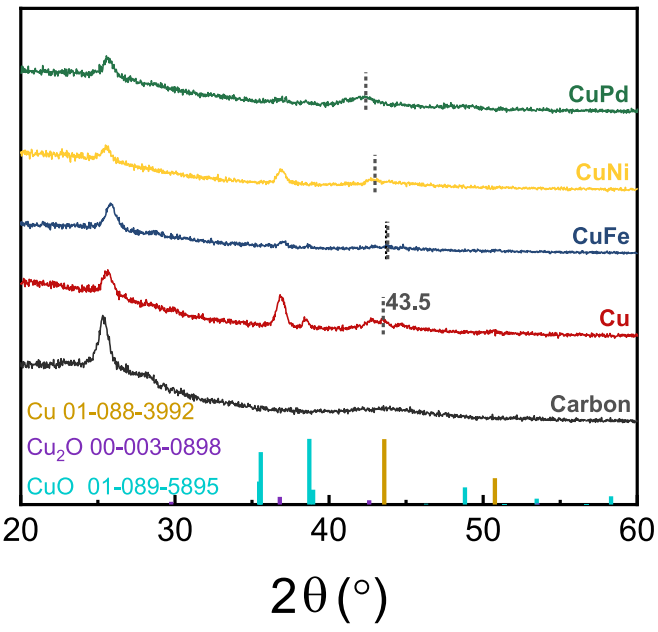

Fig. 3. XRD patterns of various metallic catalysts after Joule heating process.

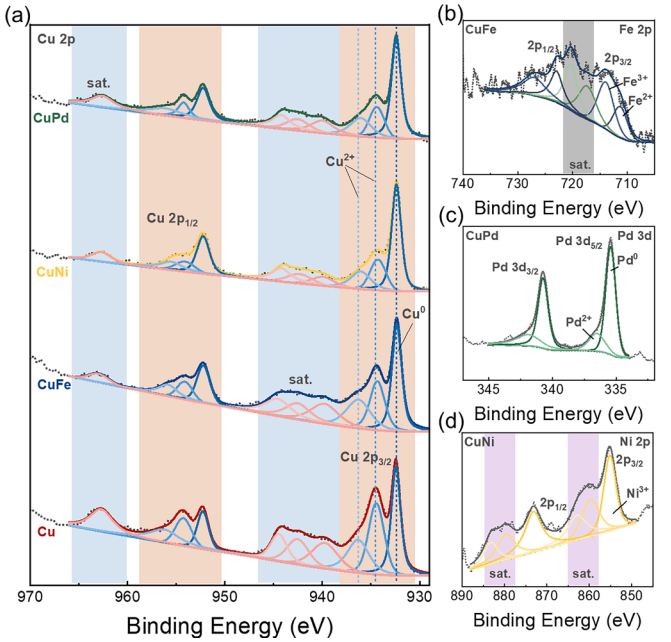

Fig. 4. (a) XPS Cu 2p spectra of 4 samples. (b) CuFe Fe 2p spectra. (c) CuPd Pd 3d spectra. (d) CuNi Ni 2p spectra.

respectively, which are lower than the typical Joule heating temperature (>1500 K) [48–50]. This suggests that the Joule heating method can be effectively extended for the synthesis of other bimetallic particles from their precursors such as $PdCl_2$ (T_d = 948 K) [51] and $FeCl_3$ (T_d = 590 K) [52]. In this study, three different bimetallic particles were synthesized including CuNi, copper-iron (CuFe), and copper-palladium (CuPd) under the same Joule heating parameters (3.2 A for 6 s). For comparison purposes, the monometallic Cu particles were also prepared as the control sample. Fig. 2 presents the SEM images and corresponding EDS mappings of the fabricated Cu, CuFe, CuNi, and CuPb particles. The SEM images confirm that all particles synthesized via the Joule heating process exhibit a similar size range of 200–400 nm. Elemental mapping further indicates a uniform distribution of each element without phase

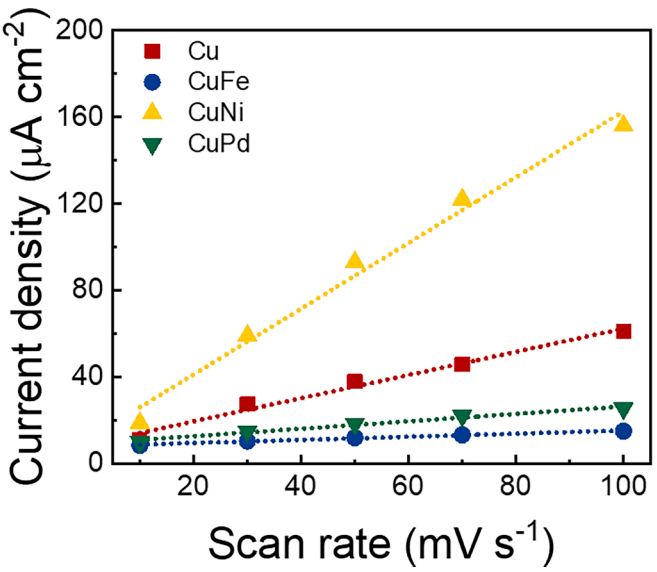

Fig. 5. The capacitance of the double layer for Cu, CuFe, CuNi, and CuPd catalysts.

separation into individual metals. These findings suggest that the Joule heating method enhances the intermetallic mixing, facilitating the synthesis of homogeneous bimetallic particles while overcoming the inherent immiscibility in bimetallic systems.

X-ray diffraction analysis (XRD) was conducted to characterize the crystalline structure of synthesized particles as shown in Fig. 3. The diffraction patterns of all samples exhibit an identical peak at 2θ of 26.2°, corresponding to the graphitic carbon [53]. Furthermore, all samples demonstrate prominent peaks from 35° to 40°, which are attributed to the oxidation of metal particles under ambient environments [54,55]. A minor peak at 43.5° corresponds to the (111) crystal plane of metallic Cu [56]. The slight shifting in diffraction peaks around 43.5° (highlighted by gray dash lines in Fig. 3 and **S6**) for bimetallic samples indicates the successful incorporation of secondary metals, i.e. Ni, Fe, and Pd. The absence of addition peaks corresponding to these secondary metals further verifies that they do not segregate to form separate phases but are well-distributed within the Cu crystalline lattice, supporting the EDS results in Fig. 2.

The surface chemical composition of different catalysts is characterized by X-ray photoelectron spectroscopy (XPS), with the spectra of individual metals shown in Fig. 4. The Cu 2p spectra of four samples can be deconvoluted into Cu $2p_{1/2}$ and Cu $2p_{3/2}$. The Cu $2p_{1/2}$ signal exhibits a characteristic feature corresponding to metallic Cu^0, with a main photoemission peak located at ~ 932.5 eV, which is the same binding energy as copper monoxide (Cu^+) [57], as depicted in Fig. 4a. The incorporation of other metals into Cu causes this peak to slightly blue shift, particularly in CuFe, and CuNi samples, which can be attributed to electron redistribution within these materials [25,58]. Two additional peaks appear alongside the Cu^+ peak, at 933.81 and 935.05 eV, indicating the presence of an oxidized compound with Cu^{2+} chemical state. The satellite (sat.) features around 940 ~ 945 eV, associated with Cu^{2+}, are clearly observed [57]. Notably, the intensities of Cu^{2+} –related signals (sat. emission peaks) are higher in the Cu sample but gradually decrease in the bimetallic samples, with the lowest intensity observed in the CuNi sample. This finding is resulted from the incorporation of a second metal element, which limits the oxidation in the bimetallic sample [20,32,59]. The CuFe sample exhibits Fe 2p spectra with binding energy ranging from 705 to 740 eV, including Fe $2p_{3/2}$ and Fe $2p_{1/2}$ (Fig. 4**b**). The observed peaks, including the sat. peaks, are a convolution of Fe signals with different oxidation states (Fe^{2+} and Fe^{3+}) [60,61]. Similarly, the Pd 3d spectra clearly indicate the presence of Pd in the CuPd sample (Fig. 4**c**). The binding energies of Pd $3d_{5/2}$ (335.8 and 337.3 eV) are lower than those of Pd $3d_{3/2}$ (341.0 and 342.5 eV) for each doublet [62]. The intense doublet peaks correspond to Pd^0, while the weaker peaks are attributed to Pd^{2+}. For the CuNi sample, the Ni 2p XPS spectra, with deconvoluted peaks for $2p_{3/2}$ and $2p_{1/2}$, exhibit multiplet splitting around 855 eV and 873 eV (Fig. 4**d**) [63,64]. These peaks indicate the presence of Ni^{3+}, likely due to the partial oxidation commonly observed in transition metal-based compounds.

Table 1
Double layer capacitance and ECSA for various Cu catalysts.

Electrodes	C_{dl} (mF cm^{-2})	ECSA
Cu	0.536	13.4
CuFe	0.072	1.80
CuNi	1.518	38.0
CuPd	0.172	4.30

To elucidate the available electrochemical active sites on the catalyst surface, cyclic voltammetry (CV) measurements were employed to scan the potential area of the non-faradaic reaction at different scan rates of 10, 30, 50, 70, and 100 mV s^{-1}. The polarization curves in **Fig. S7** exhibit an increase in current density with increasing scan rates. The absence of redox reaction within the potential range of 0——0.45 V indicates that the generated current is non-Faradaic. This finding confirms that the catalyst undergoes only adsorption and desorption reactions. The differences in current density at the middle potential versus the scan rates are plotted in Fig. 5, and the derived slope gives the electrical double-layer capacitance, C_{dl}, using **Equation S1** as reported in Table 1. It can be observed that the CuNi catalyst exhibits the highest C_{dl} of 1.518 mF cm^{-2} among different Cu-based catalysts. Assuming a specific capacitance (C_s) of 40 μF cm^{-2}, the ECSA of CuNi catalyst, calculated using **Equation S2**, is substantially larger than those of Cu, CuFe, and CuPd samples. This finding suggests a higher density of electrochemical active sites on the CuNi catalyst, revealing a potential for enhanced catalytic activity in NO_3RR.

3.2. Nitrate reduction reactions

3.2.1. Performance of different catalyst

The as-synthesized Cu-based bimetallic particles are further investigated as electrocatalysts for NO_3RR in an H-type three-electrode system (**Fig. S3**). A concentration of approximately 10 mM (~620 ppm) of NO_3^- is used in all tests to simulate NO_3^- contaminated wastewater from sources like explosives manufacturing and surface treatment industries. As a preliminary investigation, CuNi samples were synthesized using the Joule heating method at a current of 3.2 A for 6, 8, and 10 s, denoted as 6–CuNi, 8–CuNi, and 10–CuNi, respectively. Among these, the 6–CuNi catalyst demonstrates the highest NO_3RR performance, achieving superior NO_3^- conversion, NH_4^+ selectivity, and NH_4^+ yield compared to the 8 and 10-second counterparts (**Fig. S8**). The declined performance observed in catalysts subjected to longer heating times likely resulted from severe particle aggregation, as evidenced in **Fig. S9**. This aggregation reduces the available active surface area, thereby limiting the efficiency of the reduction reaction. Accordingly, the Joule heating duration of 6 s is employed for different metallic catalysts in further testing.

An additional preliminary test was performed to compare CuNi catalysts synthesized via the Joule heating process with those prepared using a conventional heating method, where the metal precursors were heated on a GDL substrate at 1000 °C for 2 h. As illustrated in **Fig. S10**a, the CuNi bimetallic particles synthesized via conventional heating exhibit a significantly larger size of approximately 6 μm, which is substantially greater than those produced through the Joule heating process (200–400 nm). Furthermore, the NO_3RR performance shown in **Fig. S10**b demonstrates that the homogeneous CuNi bimetallic particles synthesized through Joule heating outperform those prepared by the conventional method in terms of NO_3^- conversion, NH_4^+ selectivity, and

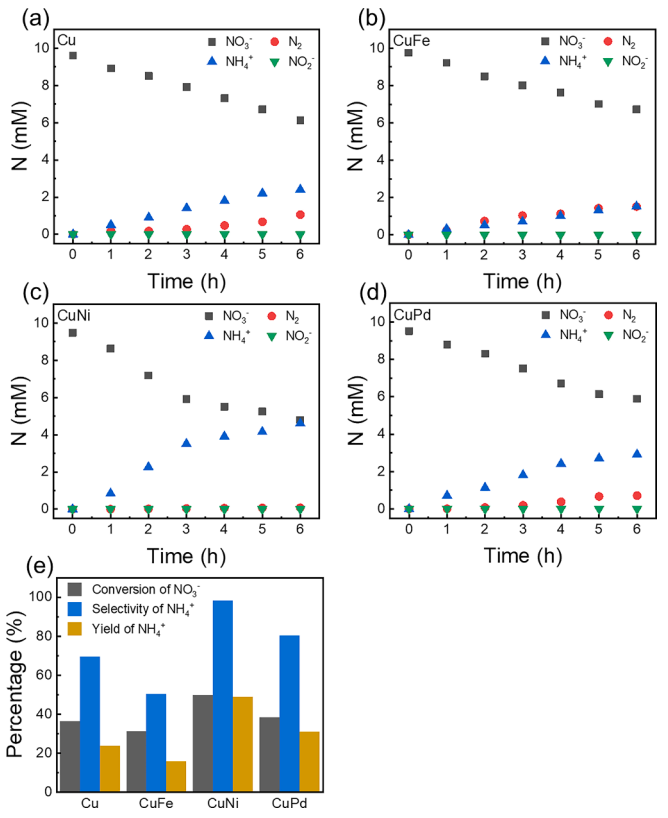

Fig. 6. NO_3RR performance of different metallic catalysts (a) Cu, (b) CuFe, (c) CuNi, and (d) CuPd. (e) Comparison of NO_3^- conversion, NH_4^+ selectivity, and NH_4^+ yield. Experimental conditions: $[HClO_4]$ = 0.1 M, $[NaNO_3]$ = 0.01 M, Applied potential = -0.9 V (vs. SCE), Temperature = 298 K.

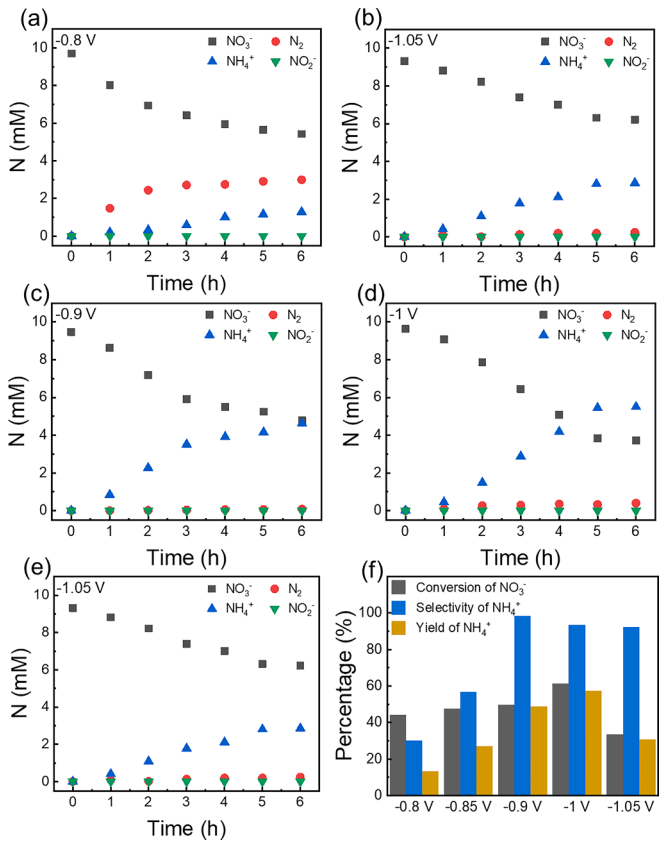

Fig. 7. Concentration profiles of N-species for NO_3RR over homogeneous CuNi catalyst at different potentials (vs. SCE). (a) −0.8 V, (b) −0.85 V, (c) 0.9 V, (d) −1.0 V, and (e) −1.05 V. (f) Summary of reduction performance. Experimental conditions: $[HClO_4]$ = 0.1 M, $[NaNO_3]$ = 0.01 M, Temperature = 298 K.

NH_4^+ yield. This result highlights the significant advantage of Joule heating process and the homogeneity of bimetallic catalysts in enhancing catalytic activity.

To explore the effects of secondary metal on NO_3RR, the change in the concentrations of NO_3^-, NO_2^-, N_2, and NH_4^+ during the reaction with different bimetallic catalysts is illustrated in Fig. 6. In all cases, almost no NO_2^- can be detected, indicating a rapid conversion. Additionally, it is observed that the NO_3^- concentration decreases as a function of time, accompanied by a clear generation of N_2 and NH_4^+, confirming the successful NO_3^- conversion (The detailed reduction mechanism will be discussed in section 3.3). It is noted that the pH of the electrolyte solution was monitored throughout the 6-hour reaction (**Table S1**). The data confirm that the reduction process occurred entirely under acidic conditions. The negligible variation in pH is likely due to the initially low pH of the solution (high concentration of H^+ ions), along with the sustained H^+ replenishment from the concurrent oxidation of H_2O in the anodic chamber [56,65].

The performance of the NO_3RR is further summarized in Fig. 6e and **Table S2**, in which the analytical values are calculated using **Equations S3-S6** in the **Supporting Information S1**. The CuNi catalyst demonstrates superior reduction performance in terms of NO_3^- conversion (50 %), NH_4^+ selectivity (98 %), and NH_4^+ yield (49 %) compared to Cu, CuFe, and CuPd. These results indicate that CuNi catalysts exhibit higher reactivity for NO_3^- reduction toward NH_4^+ production. However, the reduction performance of these four catalysts does not fully correlate with their ECSA results. To gain deeper insights into the underlying factors, the current profiles of the catalysts during NO_3RR were recorded and are presented in **Fig. S11**. The current profiles reveal distinct behaviors among the catalysts. For CuFe and CuNi, the current rises sharply at the initial stage and then stabilizes throughout the reaction. In contrast, Cu and CuPd exhibit a progressive decline in current following the initial increase phase. It is noted that the reduction potentials of Cu of Pd are relatively high ($Cu^{2+}+2e^- \rightarrow Cu$, $E^0 = 0.34$ V; $Pd^{2+}+2e^- \rightarrow Pd$, $E^0 = 0.915$ V), limiting their reduction performance after electron loss during the initial NO_3^- reduction process. This leads to a gradual decrease in reaction current. In contrast, Fe and Ni have low reduction potentials ($Fe^{2+}+2e^- \rightarrow Fe$, $E^0 = -0.44$ V; $Ni^{2+}+2e^- \rightarrow Ni$, $E^0 = -0.257$ V), enabling continuous reduction in solution, thereby maintaining a steady reaction current. In addition, the CuNi sample exhibits electron redistribution, as shown in Fig. 4a. This phenomenon indicates a decrease in anti-bonding occupation and stronger adsorbate bonding, suggesting that CuNi sample significantly enhances the adsorption energies of intermediate species [25,66]. Taken together, the exceptional catalytic activity of homogenous CuNi can mainly be attributed to the inherent electrochemical features of incorporated Ni.

3.2.2. *Performance of CuNi catalyst at different potentials*

To further investigate the NH_4^+ production process, the NO_3RR over homogeneous CuNi catalysts was also conducted under various reduction potentials from −0.8 V to −1.05 V (vs. SCE). As shown in **Fig. S12**, the reaction current density significantly increases with greater applied potentials. This trend can be explained by the direct proportional relationship between current and voltage under a constant resistance. A slight rise in pH is observed across all tests (**Table S3**), indicating the continuous consumption of H^+ ions in the solution throughout the NO_3RR process. The concentration profiles of associated NO_3RR at different potentials are illustrated in Fig. 7 and **Table S4**. The NO_3^- concentration progressively decreases without detectable NO_2^- formation, while NH_4^+ production steadily increases as the potential shifts from −0.8 to −1.0 V, followed by a sharp decline at −1.05 V potentially due to the competing hydrogen evolution reaction (HER) [19,67]. The

results demonstrate that the highest NO_3^- conversion (61 %) and NH_4^+ yield (57 %) are achieved at a reaction potential of −1.0 V while the maximum NH_4^+ selectivity (98 %) is obtained at −0.9 V. The utmost performance in terms of NH_4^+ Faradaic efficiency and formation rate is also achieved at −0.9 V, with values of 40 % and 764 μg h^{-1} cm^{-2}, respectively. This result suggests that the competing adsorption of protons with NO_3^- begins to impact the reduction performance at more negative potentials beyond −0.9 V. Additionally, this level of selectivity surpasses that reported in many previous studies (Table S5), highlighting the exceptional performance of the catalyst developed in this work.

3.3. Reduction reaction mechanism

To explore the catalytic mechanism, the following reaction steps are proposed based on the experimental results. At the beginning of the reaction, NO_3^- and H^+ ions from the solution are adsorbed onto the catalyst surface, represented as θNO_3^- and θH^+, respectively. Following this adsorption, a sequence of reduction processes occurs, converting θNO_3^- into various nitrogen-based intermediates, which eventually lead to the formation of NH_4^+ ions. These processes can be described by the equations below.

$$NO_3^- + \theta \leftrightarrows \theta NO_3^- \quad (1)$$

$$H^+ + \theta \leftrightarrows \theta H^+ \quad (2)$$

$$\theta H^+ + e^- \rightarrow \theta H \quad (3)$$

$$\theta NO_3^- + 2\theta H \rightarrow \theta NO_2^- + \theta H_2O + \theta \quad (4)$$

$$\theta NO_2^- + \theta H \rightarrow \theta NO + \theta OH^- \quad (5)$$

$$\theta NO + \theta \rightarrow \theta N + \theta O \quad (6)$$

$$\theta N + \theta N \rightarrow \theta N_2 + \theta \quad (7)$$

$$\theta N_2 \rightarrow N_2 + \theta \quad (8)$$

$$\theta NO + \theta H \rightarrow \theta NOH + \theta \quad (9)$$

$$\theta NOH + \theta H \rightarrow \theta NHOH + \theta \quad (10)$$

$$\theta NHOH + \theta H \rightarrow \theta NH + \theta H_2O \quad (11)$$

$$\theta NH + \theta H \rightarrow \theta NH_2 + \theta \quad (12)$$

$$\theta NH_2 + \theta H \rightarrow \theta NH_3 + \theta \quad (13)$$

$$\theta NH_3 \rightarrow NH_3 + \theta \quad (14)$$

$$\theta NO_2^- \leftrightarrows NO_2^- + \theta \quad (15)$$

$$NH_3 + H_2O \leftrightarrows NH_4^+ + OH^- \quad (16)$$

The concentration profiles of NO_3^-, NO_2^-, N_2, and NH_4^+ can then be expressed as the following equations, and the detailed derivation is provided in the Supporting Information S2.

$$C_{NO_3^-} = C^0_{NO_3^-} e^{-k_I t} \quad (17)$$

$$C_{NO_2^-} = \frac{k_I C^0_{NO_3^-}}{k_{II} - k_I}\left(e^{-k_I t} - e^{-k_{II} t}\right) \quad (18)$$

$$C_{N_2} = \frac{k_{III} C^0_{NO_3^-}}{k_{II} - k_I}\left(1 - e^{-k_I t}\right) + \frac{k_I k_{III} C^0_{NO_3^-}}{k_{II}(k_{II} - k_I)}\left(e^{-k_{II} t} - 1\right) \quad (19)$$

$$C_{NH_4^+} = \frac{k_V C^0_{NO_3^-}}{k_{II} - k_I}\left(1 - e^{-k_I t}\right) + \frac{k_I k_V C^0_{NO_3^-}}{k_{II}(k_{II} - k_I)}\left(e^{-k_{II} t} - 1\right) \quad (20)$$

in which

Table 2
Reaction rate constants of NO_3RR over various Cu catalysts.

Electrodes	k_I (h^{-1})	k_{II} (h^{-1})	k_{III} (h^{-1})	k_V (h^{-1})
Cu	0.07	22.6	4.30	16.6
CuFe	0.06	32.3	17.7	15.2
CuNi	0.13	22.0	0.27	22.5
CuPd	0.08	20.6	3.15	18.1

$$k_I = \frac{k_4 k_1^+ C_\theta C^2_{\theta H}}{k_1^- + k_4 C^2_{\theta H}} \quad (21)$$

$$k_{II} = \frac{k_5 C_{\theta H} C_\theta (k_6 C_\theta + k_9 C_{\theta H})}{(k_6 C_\theta + k_9 C_{\theta H}) K_{15}} \quad (22)$$

$$k_{III} = \frac{k_6 k_5 C_{\theta H} C^2_\theta}{(k_6 C_S + k_9 C_{\theta H}) K_{15}} \quad (23)$$

$$k_V = \frac{k_9 k_5 C^2_{\theta H} C_\theta K_{16}}{(k_6 C_\theta + k_9 C_{\theta H}) K_{15} C_{OH^-}} \quad (24)$$

The derived **Eqs. (17)–(20)** are applied to fit the concentration data for NO_3RR over homogeneous CuNi catalysts at −0.9 V (Fig. S13). The close agreement between the fitted results and experimental data in Fig. S13 validates the proposed NO_3RR mechanism in this study. Additionally, the kinetic constants k_I, k_{II}, k_{III}, k_V for various Cu-based catalysts are determined using the minimal residual method and the corresponding values are provided in Table 2. Here, k_I represents the rate constant for the NO_3^- removal, k_{II} refers to the NO_2^- dissociation, k_{III} reflects the balance between deoxygenation (k_5 and k_6) and hydrogenation (k_9) of nitrogen-intermediates, while k_V denotes the rate constant for the NH_4^+ formation. The results indicate that incorporating Ni into Cu catalysts enhances the NO_3^- removal rate (k_I), whereas the presence of Fe and Pd has a negligible effect. Furthermore, the value of k_{III} serves as a key determinant of the reaction pathway, influencing whether the process favors N_2 or NH_4^+ formation. A lower k_{III} value in homogeneous CuNi indicates a larger k_9 value and suggests a stronger preference for the hydrogenation of adsorbed NO intermediates, leading to enhanced selectivity for NH_4^+ over N_2. This observation can be further supported by the density functional theory (DFT) calculations from the literature [68], which report a significantly lower activation energy of θNO →θNOH (0.08 eV) compared to θNO →θN (1.62 eV). The increased k_V values observed in CuNi and CuPd compared to Cu indicate a more favorable pathway for NH_4^+ formation, aligning well with the experimental results presented in Fig. 6.

4. Conclusions

In summary, a series of homogeneous Cu-based bimetallic catalysts have been successfully synthesized through a rapid Joule heating process and applied to electrochemical NO_3^- reduction toward NH_4^+ production. Among them, CuNi showed the highest NO_3^- conversion (50 %), NH_4^+ selectivity (98 %) and NH_4^+ yield (49 %), outperforming CuFe, CuPd, and pure Cu. The enhanced performance is attributed to the synergistic interaction and electronic redistribution between Cu and Ni, which increase surface-active sites, suppress Cu oxidation, and thus improve reduction performance. This work demonstrates the advantages of uniformly-dispersed bimetallic particles in catalytic applications and presents a rapid and efficient route for developing effective and stable catalysts for wastewater treatment.

Declaration of competing interest

The authors declare that they have no known competing financial interests or personal relationships that could have appeared to influence the work reported in this paper.

Acknowledgment

This work is supported by the National Science and Technology Council of Taiwan (112-2221-E-182-070-MY3). M.-S. Hoang acknowledges the funding support from the National Science and Technology Council of Taiwan with project number 113-2811-E-182-009-MY2. The authors also acknowledge the support from the Center for Sustainability and Energy Technologies at Chang Gung University (URRPD2Q0031). XPS measurements are supported by National Science and Technology of Taiwan (114-2740-M-002-004, ESCA003500). Additionally, we thank Mr. Kong You Lai for the preliminary studies at Tamkang University.

Appendix A. Supplementary material

Supplementary data to this article can be found online at https://doi.org/10.1016/j.seppur.2025.133312.

References

[1] J. Brightling, Ammonia and the fertiliser industry: the development of ammonia at billingham, Johnson Matthey Technol. Rev. 62 (2018) 32–47, https://doi.org/10.1595/205651318X696341.
[2] J.G. Chen, R.M. Crooks, L.C. Seefeldt, K.L. Bren, R.M. Bullock, M.Y. Darensbourg, P.L. Holland, B. Hoffman, M.J. Janik, A.K. Jones, M.G. Kanatzidis, P. King, K. M. Lancaster, S.V. Lymar, P. Pfromm, W.F. Schneider, R.R. Schrock, Beyond fossil fuel–driven nitrogen transformations, Science 360 (2018) eaar6611, https://doi.org/10.1126/science.aar6611.
[3] J. Guo, P. Chen, Catalyst: NH3 as an energy carrier, Chem. 3 (2017) 709–712, https://doi.org/10.1016/j.chempr.2017.10.004.
[4] Y. Wang, S. Zheng, J. Chen, Z. Wang, S. He, Ammonia (NH3) storage for massive PV electricity, Energy Procedia 150 (2018) 99–105, https://doi.org/10.1016/j.egypro.2018.09.001.
[5] R. Lan, J.T.S. Irvine, S. Tao, Ammonia and related chemicals as potential indirect hydrogen storage materials, Int. J. Hydrogen Energy 37 (2012) 1482–1494, https://doi.org/10.1016/j.ijhydene.2011.10.004.
[6] B.H.R. Suryanto, H.-L. Du, D. Wang, J. Chen, A.N. Simonov, D.R. MacFarlane, Challenges and prospects in the catalysis of electroreduction of nitrogen to ammonia, Nat. Catal. 2 (2019) 290–296, https://doi.org/10.1038/s41929-019-0252-4.
[7] H. Chen, J. Liang, K. Dong, L. Yue, T. Li, Y. Luo, Z. Feng, N. Li, M.S. Hamdy, A. A. Alshehri, Y. Wang, X. Sun, Q. Liu, Ambient electrochemical N2-to-NH3 conversion catalyzed by TiO2 decorated juncus effusus-derived carbon microtubes, Inorg. Chem. Front. 9 (2022) 1514–1519, https://doi.org/10.1039/D2QI00140C.
[8] Y. Luo, Q. Li, Y. Tian, Y. Liu, K. Chu, Amorphization engineered VSe2−x nanosheets with abundant Se-vacancies for enhanced N2 electroreduction, J. Mater. Chem. A Mater. 10 (2022) 1742–1749, https://doi.org/10.1039/D1TA06746J.
[9] S. Li, Y. Luo, L. Yue, T. Li, Y. Wang, Q. Liu, G. Cui, F. Zhang, A.M. Asiri, X. Sun, An amorphous WC thin film enabled high-efficiency N2 reduction electrocatalysis under ambient conditions, Chem. Commun. 57 (2021) 7806–7809, https://doi.org/10.1039/D1CC03139B.
[10] Q. Liu, T. Xu, Y. Luo, Q. Kong, T. Li, S. Lu, A.A. Alshehri, K.A. Alzahrani, X. Sun, Recent advances in strategies for highly selective electrocatalytic N2 reduction toward ambient NH3 synthesis, Curr. Opin. Electrochem. 29 (2021) 100766, https://doi.org/10.1016/j.coelec.2021.100766.
[11] K. Chu, X. Li, Q. Li, Y. Guo, H. Zhang, Synergistic enhancement of electrocatalytic nitrogen reduction over boron nitride quantum dots decorated Nb2CT-MXene, Small 17 (2021) 2102363, https://doi.org/10.1002/smll.202102363.
[12] M. Zheng, Y. Wan, L. Yang, S. Ao, W. Fu, Z. Zhang, Z.-H. Huang, T. Ling, F. Kang, R. Lv, In situ construction of Cu(I)-Cu(II) pairs for efficient electrocatalytic nitrate reduction reaction to ammonia, J. Energy Chem. 100 (2025) 106–113, https://doi.org/10.1016/j.jechem.2024.08.020.
[13] Z. Xi, H. Hu, Q. Chen, M. Ning, S. Wang, H. Yu, Y. Sun, D.-W. Wang, H. Jin, H.-M. Cheng, 2D Catalysts for Electrocatalytic Nitrate Reduction and C-N Coupling Reactions, Adv. Funct. Mater. (2025) 2425611, https://doi.org/10.1002/adfm.202425611.
[14] X. Meng, X. Tan, Y. Ma, A.A. Obisanya, J. Wang, Z. Xiao, D. Wang, Recent progress in cobalt-based electrocatalysts for efficient electrochemical nitrate reduction reaction, Adv. Funct. Mater. 35 (2025) 2418492, https://doi.org/10.1002/adfm.202418492.
[15] R. Zhang, X. Ma, S. Zhang, Q. Li, Y. Zhao, C. Zhi, Alloy catalysts for electrochemical nitrate reduction to ammonia, Chem. Electro. Chem. 12 (2025) e202400499, https://doi.org/10.1002/celc.202400499.
[16] Y. Han, X. Zhang, W. Cai, H. Zhao, Y. Zhang, Y. Sun, Z. Hu, S. Li, J. Lai, L. Wang, Facet-controlled palladium nanocrystalline for enhanced nitrate reduction towards ammonia, J. Colloid Interface Sci. 600 (2021) 620–628, https://doi.org/10.1016/j.jcis.2021.05.061.
[17] J. Wu, Y.-X. Yu, Highly selective electroreduction of nitrate to ammonia on a Ru-doped tetragonal Co2P monolayer with low-limiting overpotential, Catal. Sci. Technol. 11 (2021) 7160–7170, https://doi.org/10.1039/D1CY01217G.
[18] S. Yeon, S.J. Lee, J. Kim, T. Begildayeva, A. Min, J. Theerthagiri, M.L.A. Kumari, L. M.C. Pinto, H. Kong, M.Y. Choi, Sustainable removal of nitrite waste to value-added ammonia on Cu@Cu2O core–shell nanostructures by pulsed laser technique, Environ. Res. 215 (2022) 114154, https://doi.org/10.1016/j.envres.2022.114154.
[19] J.F. Su, Y.C. Ye, Facet engineering of polycrystalline copper catalytic electrode through additive-assisted electrodeposition for nitrate reduction to ammonium, Sep. Purif. Technol. 363 (2025) 132206, https://doi.org/10.1016/j.seppur.2025.132206.
[20] K. Zhang, Y. Liu, Z. Pan, Q. Xia, X. Huo, O.C. Esan, X. Zhang, L. An, Cu-based catalysts for electrocatalytic nitrate reduction to ammonia: fundamentals and recent advances, EES Catal. 2 (2024) 727–752, https://doi.org/10.1039/D4EY00002A.
[21] Z. Ma, C. Wang, T. Yang, G. Wei, J. Huang, M. Liu, K. Zhang, Z. Zhang, Y. Liu, S. Gao, A 3D porous P-doped Cu–Ni alloy for atomic H* enhanced electrocatalytic reduction of nitrate to ammonia, J. Mater.Chem A Mater 12 (2024) 7654–7662, https://doi.org/10.1039/D3TA08086B.
[22] S.-X. Wei, Y.-H. Yang, X.-B. Liu, X.-B. Ye, X.-P. Zhao, X.-W. Pi, X.-F. Cheng, J.-H. He, Laser-induced PdCu alloy catalysts for highly efficient and stable electrocatalytic nitrate reduction to ammonia, J. Colloid Interface Sci. 689 (2025) 137202, https://doi.org/10.1016/j.jcis.2025.02.210.
[23] K. Zhang, G. Wei, Z. Zhang, Z. Zhao, C. Wu, Y. Liu, Y. Yang, Y. Chen, Construction of ternary alloy Cu-Ni-Co catalysts with highly active sites to enhance the initial adsorption process of nitrate reduction to ammonia, Electrochim. Acta 486 (2024) 144124, https://doi.org/10.1016/j.electacta.2024.144124.
[24] G.A. Cerrón-Calle, A.S. Fajardo, C.M. Sánchez-Sánchez, S. Garcia-Segura, Highly reactive Cu-Pt bimetallic 3D-electrocatalyst for selective nitrate reduction to ammonia, Appl. Catal. B 302 (2022) 120844, https://doi.org/10.1016/j.apcatb.2021.120844.
[25] Y. Wang, A. Xu, Z. Wang, L. Huang, J. Li, F. Li, J. Wicks, M. Luo, D.-H. Nam, C.-S. Tan, Y. Ding, J. Wu, Y. Lum, C.-T. Dinh, D. Sinton, G. Zheng, E.H. Sargent, Enhanced nitrate-to-ammonia activity on copper–nickel alloys via tuning of intermediate adsorption, J. Am. Chem. Soc. 142 (2020) 5702–5708, https://doi.org/10.1021/jacs.9b13347.
[26] Y. Sun, S. Dai, High-entropy materials for catalysis: A new frontier, Sci. Adv. 7 (2025) eabg1600, https://doi.org/10.1126/sciadv.abg1600.
[27] S. Wu, Y. Liu, Y. Ren, Q. Wei, Y. Sun, Microwave synthesis of single-phase nanoparticles made of multi-principal element alloys, Nano Res. 15 (2022) 4886–4892, https://doi.org/10.1007/s12274-021-3893-y.
[28] J.F. Su, I. Ruzybayev, I. Shah, C.P. Huang, The electrochemical reduction of nitrate over micro-architectured metal electrodes with stainless steel scaffold, Appl. Catal. B 180 (2016) 199–209, https://doi.org/10.1016/j.apcatb.2015.06.028.
[29] C. Wang, Z. Liu, T. Hu, J. Li, L. Dong, F. Du, C. Li, C. Guo, Metasequoia-like nanocrystal of iron-doped copper for efficient electrocatalytic nitrate reduction into ammonia in neutral media, Chem. Sus. Chem. 14 (2021) 1825–1829, https://doi.org/10.1002/cssc.202100127.
[30] W. Gao, K. Xie, J. Xie, X. Wang, H. Zhang, S. Chen, H. Wang, Z. Li, C. Li, Alloying of Cu with Ru enabling the relay catalysis for reduction of nitrate to ammonia, Adv. Mater. 35 (2023) 2202952, https://doi.org/10.1002/adma.202202952.
[31] X. Zheng, Y. Yan, X. Li, Y. Liu, Y. Yao, Theoretical insights into dissociative-associative mechanism for enhanced electrochemical nitrate reduction to ammonia, J. Hazard. Mater. 446 (2023) 130679, https://doi.org/10.1016/j.jhazmat.2022.130679.
[32] Y. Chen, Y. Zhao, Z. Zhao, Y. Liu, Highly dispersed face-centered cubic copper–cobalt alloys constructed by ultrafast carbothermal shock for efficient electrocatalytic nitrate-to-ammonia conversion, Mater. Today Energy 29 (2022) 101112, https://doi.org/10.1016/j.mtener.2022.101112.
[33] X. Zhang, C. Wang, Y. Guo, B. Zhang, Y. Wang, Y. Yu, Cu clusters/TiO2−x with abundant oxygen vacancies for enhanced electrocatalytic nitrate reduction to ammonia, J. Mater. Chem. A Mater. 10 (2022) 6448–6453, https://doi.org/10.1039/D2TA00661H.
[34] W. He, J. Zhang, S. Dieckhöfer, S. Varhade, A.C. Brix, A. Lielpetere, S. Seisel, J.R. C. Junqueira, W. Schuhmann, Splicing the active phases of copper/cobalt-based catalysts achieves high-rate tandem electroreduction of nitrate to ammonia, Nat. Commun. 13 (2022) 1129, https://doi.org/10.1038/s41467-022-28728-4.
[35] K.D. Gilroy, A. Ruditskiy, H.-C. Peng, D. Qin, Y. Xia, Bimetallic nanocrystals: syntheses, properties, and applications, Chem. Rev. 116 (2016) 10414–10472, https://doi.org/10.1021/acs.chemrev.6b00211.
[36] C. Yang, B.H. Ko, S. Hwang, Z. Liu, Y. Yao, W. Luc, M. Cui, A.S. Malkani, T. Li, X. Wang, J. Dai, B. Xu, G. Wang, D. Su, F. Jiao, L. Hu, Overcoming immiscibility toward bimetallic catalyst library, Sci. Adv. 6 (2023) eaaz6844, https://doi.org/10.1126/sciadv.aaz6844.
[37] D. Wang, Y. Li, Bimetallic nanocrystals: liquid-phase synthesis and catalytic applications, Adv. Mater. 23 (2011) 1044–1060, https://doi.org/10.1002/adma.201003695.
[38] N.S. Tabrizi, Q. Xu, N.M. van der Pers, A. Schmidt-Ott, Generation of mixed metallic nanoparticles from immiscible metals by spark discharge, J. Nanopart. Res. 12 (2010) 247–259, https://doi.org/10.1007/s11051-009-9603-4.
[39] K.A. Kane, A.C. Reber, S.N. Khanna, M.F. Bertino, Laser synthesized nanoparticle alloys of metals with bulk miscibility gaps, Prog. Nat. Sci.: Mater. Int. 28 (2018) 456–463, https://doi.org/10.1016/j.pnsc.2018.05.001.
[40] Y. Chen, G.C. Egan, J. Wan, S. Zhu, R.J. Jacob, W. Zhou, J. Dai, Y. Wang, V. A. Danner, Y. Yao, K. Fu, Y. Wang, W. Bao, T. Li, M.R. Zachariah, L. Hu, Ultra-fast self-assembly and stabilization of reactive nanoparticles in reduced graphene oxide films, Nat. Commun. 7 (2016) 12332, https://doi.org/10.1038/ncomms12332.
[41] H. Wu, Q. Lu, Y. Li, J. Wang, Y. Li, R. Jiang, J. Zhang, X. Zheng, X. Han, N. Zhao, J. Li, Y. Deng, W. Hu, Rapid joule-heating synthesis for manufacturing high-

entropy oxides as efficient electrocatalysts, Nano Lett. 22 (2022) 6492–6500, https://doi.org/10.1021/acs.nanolett.2c01147.
[42] Z. Zhang, Y. Liu, X. Su, Z. Zhao, Z. Mo, C. Wang, Y. Zhao, Y. Chen, S. Gao, Electro-triggered Joule heating method to synthesize single-phase CuNi nano-alloy catalyst for efficient electrocatalytic nitrate reduction toward ammonia, Nano Res. 16 (2023) 6632–6641, https://doi.org/10.1007/s12274-023-5402-y.
[43] J.-H. Cha, S.-H. Cho, D.-H. Kim, D. Jeon, S. Park, J.-W. Jung, I.-D. Kim, S.-Y. Choi, Flash-thermal shock synthesis of high-entropy alloys toward high-performance water splitting, Adv. Mater. 35 (2023) 2305222, https://doi.org/10.1002/adma.202305222.
[44] F. Chen, Y. Yao, A. Nie, S. Xu, J. Dai, E. Hitz, Y. Li, A. Lu, Z. Huang, T. Li, R. Shahbazian-Yassar, L. Hu, High-temperature atomic mixing toward well-dispersed bimetallic electrocatalysts, Adv. Energy Mater. 8 (2018) 1800466, https://doi.org/10.1002/aenm.201800466.
[45] Y. Yao, Z. Huang, P. Xie, S.D. Lacey, R.J. Jacob, H. Xie, F. Chen, A. Nie, T. Pu, M. Rehwoldt, D. Yu, M.R. Zachariah, C. Wang, R. Shahbazian-Yassar, J. Li, L. Hu, Carbothermal shock synthesis of high-entropy-alloy nanoparticles, Science 359 (2018) 1489–1494, https://doi.org/10.1126/science.aan5412.
[46] S. Zhou, S. Shen, D. Zhao, Z. Zhang, S. Yan, Evaporation and decomposition of eutectics of cupric chloride and sodium chloride, J. Therm. Anal. Calorim. 129 (2017) 1445–1452, https://doi.org/10.1007/s10973-017-6360-y.
[47] S.K. Mishra, S.B. Kanungo, Thermal dehydration and decomposition of nickel chloride hydrate (NiCl2·xH2O), J. Therm. Anal. 38 (1992) 2417–2436, https://doi.org/10.1007/BF01974621.
[48] W. Bao, A.D. Pickel, Q. Zhang, Y. Chen, Y. Yao, J. Wan, K. Fu, Y. Wang, J. Dai, H. Zhu, D. Drew, M. Fuhrer, C. Dames, L. Hu, Flexible, high temperature, planar lighting with large scale printable nanocarbon paper, Adv. Mater. 28 (2016) 4684–4691, https://doi.org/10.1002/adma.201506116.
[49] Y. Yao, K.K. Fu, S. Zhu, J. Dai, Y. Wang, G. Pastel, Y. Chen, T. Li, C. Wang, T. Li, L. Hu, Carbon welding by ultrafast joule heating, Nano Lett. 16 (2016) 7282–7289, https://doi.org/10.1021/acs.nanolett.6b03888.
[50] T. Li, Q. Dong, Z. Huang, L. Wu, Y. Yao, J. Gao, X. Wang, H. Zhang, D. Wang, T. Li, R. Shahbazian-Yassar, L. Hu, Interface engineering between multi-elemental alloy nanoparticles and a carbon support toward stable catalysts, Adv. Mater. 34 (2022) 2106436, https://doi.org/10.1002/adma.202106436.
[51] M. Cui, C. Yang, S. Hwang, M. Yang, S. Overa, Q. Dong, Y. Yao, A.H. Brozena, D. A. Cullen, M. Chi, T.F. Blum, D. Morris, Z. Finfrock, X. Wang, P. Zhang, V. G. Goncharov, X. Guo, J. Luo, Y. Mo, F. Jiao, L. Hu, Multi-principal elemental intermetallic nanoparticles synthesized via a disorder-to-order transition, Sci. Adv. 8 (2025) eabm4322, https://doi.org/10.1126/sciadv.abm4322.
[52] S.B. Kanungo, S.K. Mishra, Thermal dehydration and decomposition of FeCl3·xH2O, J. Therm. Anal. 46 (1996) 1487–1500, https://doi.org/10.1007/BF01979262.
[53] F.Y. Ban, S.R. Majid, N.M. Huang, H.N. Lim, Graphene oxide and its electrochemical performance, Int. J. Electrochem. Sci. 7 (2012) 4345–4351, https://doi.org/10.1016/S1452-3981(23)19543-5.
[54] A.K. Kar, R. Srivastava, Selective synthesis of Cu–Cu2O/C and CuO–Cu2O/C catalysts for Pd-free C–C, C–N coupling and oxidation reactions, Inorg. Chem. Front. 6 (2019) 576–589, https://doi.org/10.1039/C8QI01198B.
[55] F. Bayat, S. Sheibani, Enhancement of photocatalytic activity of CuO-Cu2O heterostructures through the controlled content of Cu2O, Mater. Res. Bull. 145 (2022) 111561, https://doi.org/10.1016/j.materresbull.2021.111561.
[56] J.F. Su, D. Mohanty, A porous copper catalyst for electrochemical nitrate reduction to ammonium, J. Environ. Chem. Eng. 13 (2025) 115596, https://doi.org/10.1016/j.jece.2025.115596.
[57] J.A. Torres-Ochoa, D. Cabrera-German, O. Cortazar-Martinez, M. Bravo-Sanchez, G. Gomez-Sosa, A. Herrera-Gomez, Peak-fitting of Cu 2p photoemission spectra in Cu0, Cu1+, and Cu2+ oxides: a method for discriminating Cu0 from Cu1+, Appl. Surf. Sci. 622 (2023) 156960 https://doi.org/10.1016/j.apsusc.2023.156960.
[58] A. Jha, D.-W. Jeong, J.-O. Shim, W.-J. Jang, Y.-L. Lee, C.V. Rode, H.-S. Roh, Hydrogen production by the water-gas shift reaction using CuNi/Fe2O3 catalyst, Catal. Sci. Technol. 5 (2015) 2752–2760, https://doi.org/10.1039/C5CY00173K.
[59] Y. Liu, B. Deng, K. Li, H. Wang, Y. Sun, F. Dong, Metal-organic framework derived carbon-supported bimetallic copper-nickel alloy electrocatalysts for highly selective nitrate reduction to ammonia, J. Colloid Interface Sci. 614 (2022) 405–414, https://doi.org/10.1016/j.jcis.2022.01.127.
[60] P. Li, Y. Xuan, B. Jiang, S. Zhang, C. Xia, Hollow La0.6Sr0.4Ni0.2Fe0.75Mo0.05O3-δ electrodes with exsolved FeNi3 in quasi-symmetrical solid oxide electrolysis cells for direct CO2 electrolysis, Electrochem. Commun. 134 (2022) 107188, https://doi.org/10.1016/j.elecom.2021.107188.
[61] K.O. Moura, R.J.S. Lima, A.A. Coelho, E.A. Souza-Junior, J.G.S. Duque, C. T. Meneses, Tuning the surface anisotropy in Fe-doped NiO nanoparticles, Nanoscale 6 (2014) 352–357, https://doi.org/10.1039/C3NR04926D.
[62] P. Wu, Y. Huang, L. Kang, M. Wu, Y. Wang, Multisource synergistic electrocatalytic oxidation effect of strongly coupled PdM (M = Sn, Pb)/N-doped graphene nanocomposite on small organic molecules, Sci. Rep. 5 (2015) 14173, https://doi.org/10.1038/srep14173.
[63] M. Cheng, H. Fan, Y. Song, Y. Cui, R. Wang, Interconnected hierarchical NiCo2O4 microspheres as high-performance electrode materials for supercapacitors, Dalton Trans. 46 (2017) 9201–9209, https://doi.org/10.1039/C7DT01289F.
[64] N.A. Saguì, P. Ström, T. Edvinsson, İ. Bayrak Pehlivan, Nickel site modification by high-valence doping: effect of tantalum impurities on the alkaline water electro-oxidation by NiO probed by operando raman spectroscopy, ACS Catal. 12 (2022) 6506–6516, https://doi.org/10.1021/acscatal.2c00577.
[65] C.-P. Huang, H.-W. Wang, P.-C. Chiu, Nitrate reduction by metallic iron, Water Res. 32 (1998) 2257–2264, https://doi.org/10.1016/S0043-1354(97)00464-8.
[66] J.K. Nørskov, F. Abild-Pedersen, F. Studt, T. Bligaard, Density functional theory in surface chemistry and catalysis, Proc. Natl. Acad. Sci. 108 (2011) 937–943, https://doi.org/10.1073/pnas.1006652108.
[67] M. Yang, B. Li, S. Li, Q. Dong, Z. Huang, S. Zheng, Y. Fang, G. Zhou, X. Chen, X. Zhu, T. Li, M. Chi, G. Wang, L. Hu, Z.J. Ren, Highly selective electrochemical nitrate to ammonia conversion by dispersed Ru in a multielement alloy catalyst, Nano Lett. 23 (2023) 7733–7742, https://doi.org/10.1021/acs.nanolett.3c01978.
[68] T. Hu, C. Wang, M. Wang, C.M. Li, C. Guo, Theoretical insights into superior nitrate reduction to ammonia performance of copper catalysts, ACS Catal 11 (2021) 14417–14427, https://doi.org/10.1021/acscatal.1c03666.